

Nonlinear Noise2Noise for Efficient Monte Carlo Denoiser Training

ANDREW TINITS, University of Waterloo, Canada
STEPHEN MANN, University of Waterloo, Canada

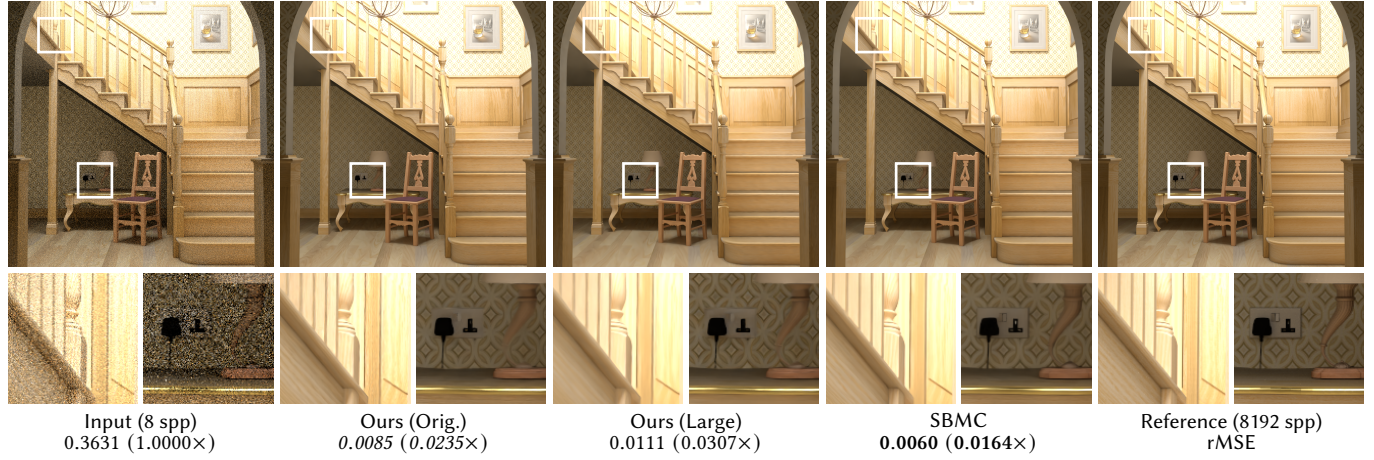


Fig. 1. A Monte Carlo rendering at 8 samples per pixel (spp), denoised with our models, denoised with the SBMC model, and the reference image rendered at 8192 spp. Our models are trained with only noisy data, while SBMC is trained with clean reference images. (The Wooden Staircase by Wig42, CC BY 3.0)

The Noise2Noise method allows for training machine learning-based denoisers with pairs of input and target images where both the input and target can be noisy. This removes the need for training with clean target images, which can be difficult to obtain. However, Noise2Noise training has a major limitation: nonlinear functions applied to the noisy targets will skew the results. This bias occurs because the nonlinearity makes the expected value of the noisy targets different from the clean target image. Since nonlinear functions are common in image processing, avoiding them limits the types of preprocessing that can be performed on the noisy targets. Our main insight is that certain nonlinear functions can be applied to the noisy targets without adding significant bias to the results. We develop a theoretical framework for analyzing the effects of these nonlinearities, and describe a class of nonlinear functions with minimal bias.

We demonstrate our method on the denoising of high dynamic range (HDR) images produced by Monte Carlo rendering, where generating high-sample count reference images can be prohibitively expensive. Noise2Noise training can have trouble with HDR images, where the training process is overwhelmed by outliers and performs poorly. We consider a commonly used method of addressing these training issues: applying a nonlinear tone mapping function to the model output and target images to reduce their dynamic range. This method was previously thought to be incompatible with Noise2Noise training because of the nonlinearities involved. We show that certain combinations of loss functions and tone mapping functions can reduce the effect of outliers while introducing minimal bias. We apply our

Authors' Contact Information: Andrew Tinitis, University of Waterloo, Waterloo, Ontario, Canada, amtinitis@uwaterloo.ca; Stephen Mann, University of Waterloo, Waterloo, Ontario, Canada, sman@uwaterloo.ca.



This work is licensed under a Creative Commons Attribution 4.0 International License.
SA Conference Papers '25, Hong Kong, Hong Kong
© 2025 Copyright held by the owner/author(s).
ACM ISBN 979-8-4007-2137-3/2025/12
<https://doi.org/10.1145/3757377.3763931>

method to an existing machine learning-based Monte Carlo denoiser, where the original implementation was trained with high-sample count reference images. Our results approach those of the original implementation, but are produced using only noisy training data.

CCS Concepts: • Computing methodologies → Image processing; Ray tracing; Neural networks.

Additional Key Words and Phrases: Noise2Noise, nonlinear functions, Jensen gap, Monte Carlo denoising, high dynamic range, tone mapping

ACM Reference Format:

Andrew Tinitis and Stephen Mann. 2025. Nonlinear Noise2Noise for Efficient Monte Carlo Denoiser Training. In *SIGGRAPH Asia 2025 Conference Papers (SA Conference Papers '25), December 15–18, 2025, Hong Kong, Hong Kong*. ACM, New York, NY, USA, 15 pages. <https://doi.org/10.1145/3757377.3763931>

1 Introduction

There are many applications in image processing where clean images are hard to obtain, such as with long-exposure photography or Monte Carlo rendering. In these cases, the noise is gradually reduced through a lengthy process, making clean images expensive to produce. Denoising offers a solution to this problem, where the image generating process can be stopped before convergence, and post-processing techniques can be applied to reduce the remaining noise to an acceptable level. Denoising has contributed to recent successes in adapting Monte Carlo rendering for real-time applications, for example. Common denoising methods use either hand-tuned filters or machine learning models to reduce the noise.

Learning-based denoisers are trained on large datasets of images and their associated feature data. In the supervised learning setting, these datasets contain pairs of noisy images with their corresponding clean reference images. However, difficulty in obtaining clean

references presents a challenge to training denoisers with supervised learning. A potential solution to this problem is to remove the need for clean reference images by changing to a different learning setting where clean references are not required. One such method is Noise2Noise, a weakly supervised learning approach where denoisers are trained with pairs of noisy images [Lehtinen et al. 2018]. For the common case where the noise distribution has zero mean, Noise2Noise is used with the L_2 loss to recover the expectation of the noisy targets $\mathbb{E}[\hat{y}]$, which is equal to the clean target y [Lehtinen et al. 2018]. The error from the noisy targets approaches zero as the number of training examples increases [Lehtinen et al. 2018].

Noise2Noise, in the zero-mean noise setting, has a major limitation: nonlinear functions applied to the noisy targets will skew the results [Lehtinen et al. 2018]. This bias occurs because the nonlinearity φ makes the expected value of the noisy targets $\mathbb{E}[\varphi(\hat{y})]$ different from the clean target $\varphi(\mathbb{E}[\hat{y}])$ [Lehtinen et al. 2018], since in general $\mathbb{E}[\varphi(\hat{y})] \neq \varphi(\mathbb{E}[\hat{y}])$. Nonlinear functions are common in image processing, so the current practice of avoiding nonlinearity limits the types of preprocessing that can be performed on the noisy targets. Our main insight is that certain nonlinear functions can be applied to the noisy targets without adding significant bias to the results. We develop a theoretical framework, based on the Jensen gap $\mathbb{E}[\varphi(\hat{y})] - \varphi(\mathbb{E}[\hat{y}])$ [Jensen 1906], for analyzing the effects of these nonlinearities on Noise2Noise training. We then use our framework to describe a class of nonlinear functions with minimal bias.

Noise2Noise training has been widely adopted for other denoising problems, but has not seen wide adoption for the denoising of Monte Carlo rendered images. Monte Carlo rendering is a randomized algorithm that samples the space of possible light paths through a scene. Although this process converges in the limit to the correct image, achieving a low noise level can require many thousands of samples, which can be prohibitively expensive. Monte Carlo noise has zero mean, which makes it an ideal candidate for Noise2Noise training. However, Monte Carlo renderings often have a high dynamic range (HDR) spanning many orders of magnitude, especially at low samples per pixel (spp). Noise2Noise training can have trouble with HDR images, where the L_2 loss is overwhelmed by outliers and the training fails to converge [Lehtinen et al. 2018]. The Noise2Noise authors offer a solution to this problem with their L_{HDR} loss function [Lehtinen et al. 2018], but in our testing this solution is insufficient, and the training still performs poorly. We attribute this difference in our findings to our more complex model and our significantly larger and more varied training dataset.

One existing solution to the HDR training issues is to apply a nonlinear tone mapping function to the model output and target images to reduce their dynamic range [Gharbi et al. 2019]. This method was previously thought to be incompatible with Noise2Noise training because of the nonlinearities involved [Lehtinen et al. 2018]. We show that this method can in fact be used with Noise2Noise training. We apply our theoretical framework to show that certain combinations of loss functions and tone mapping functions can reduce the effect of outliers while introducing minimal bias to the results. Our experimental results confirm the effectiveness of this approach. We apply our method to an existing machine learning-based Monte Carlo denoiser [Gharbi et al. 2019], where the original implementation was trained with high-sample count reference images. Our

denoising results approach those of the original implementation, but are produced using only low-sample count noisy training data. Monte Carlo denoising of varied scenes with complex models is therefore an example of an application where training from noisy data is made possible by our nonlinear Noise2Noise method.

2 Related Work

2.1 Weakly Supervised Image Denoising

Noise2Noise [Lehtinen et al. 2018] was not the first work to recognize that clean reference images are not necessary for image denoising. Outside of machine learning methods, there are classic algorithms such as NLM [Buades et al. 2005] and BM3D [Dabov et al. 2007] that denoise a single noisy image without requiring any additional information. These methods look at statistical information from the rest of the image to determine how to denoise a particular pixel. Within machine learning, Noise2Noise is the first denoising method that can learn from noisy images without requiring prior knowledge of either the noise distribution or the distribution of the clean images [Lehtinen et al. 2018]. Other methods that can train on noisy images, such as AmbientGAN [Bora et al. 2018] and GradNet [Guo et al. 2019], require either an explicit statistical model of the noise (AmbientGAN), or additional regularization that makes assumptions about the clean results (GradNet). In the case of Monte Carlo denoising, the noise distribution cannot be characterized analytically, so methods with the former requirement cannot be used [Lehtinen et al. 2018].

Since the publication of Noise2Noise, several works have extended the idea so that only individual noisy images are required for training, rather than the noisy image pairs required by Noise2Noise [Lehtinen et al. 2018]. These works include Noise2Void [Krull et al. 2019], Noise2Self [Batson and Royer 2019], and the work of Laine et al. [2019]. Our idea of applying nonlinearity to the noisy targets can equally be used with these methods and others that make use of the Noise2Noise property. Single-image denoising is useful in settings where noisy image pairs are difficult to obtain, such as in biomedical imaging. However, these methods generally come with reduced performance when compared to Noise2Noise because they have less information available during training [Krull et al. 2019]. It therefore makes sense to use Noise2Noise in settings such as Monte Carlo denoising, where noisy image pairs are easy to obtain.

This work is a continuation of previous experimental work by the first author [Tinit 2022]. To our knowledge, these two works are the first to successfully apply nonlinear functions to the noisy targets in Noise2Noise training.

2.2 Monte Carlo Denoising

Monte Carlo denoising methods can be separated into two main categories: traditional algorithms, and machine learning-based methods. We briefly review machine-learning based methods below. For a more comprehensive review, see the survey papers by Zwicker et al. [2015] and Huo and Yoon [2021].

The use of machine learning for Monte Carlo denoising was initiated by Kalantari et al. [2015], who used a multi-layer perceptron (MLP) to predict the parameters of a cross-bilateral filter. Bako et al. improved this idea by using a deep convolutional neural network

(CNN) to predict filter kernels separately for each pixel [2017]. This kernel prediction idea is used by many later works [Back et al. 2020; Gharbi et al. 2019; Lin et al. 2020, 2021; Meng et al. 2020; Munkberg and Hasselgren 2020; Vogels et al. 2018]. Other recent works take the simpler approach of predicting the pixel radiances directly [Chaitanya et al. 2017; Guo et al. 2019; Lu et al. 2020; Wong and Wong 2019; Xu et al. 2019; Yang et al. 2018, 2019]. Gharbi et al. propose another alternative where splatting kernels are used to allow individual pixels to determine their own contributions [2019]. This concept is extended by Munkberg and Hasselgren [2020], who divide the samples into layers and filter them separately to improve efficiency, and by Lin et al. [2021] and Cho et al. [2021], who add information about individual Monte Carlo paths. Other recent works use different model architectures, such as generative adversarial networks (GANs) [Lu et al. 2021, 2020; Xu et al. 2019], self-attention [Chen et al. 2023, 2024; Oh and Moon 2024; Yu et al. 2021], and diffusion models [Vavilala et al. 2024]. Several works in recent years have explored unsupervised learning [Back et al. 2022; Choi et al. 2024; Guo et al. 2019; Xu et al. 2020]. Weakly supervised learning for Monte Carlo denoising was studied by Cho et al. [2021], but their method uses high-sample count reference images for training.

3 Noise2Noise Theory

The typical supervised machine learning regression task uses a model f with parameters θ , a loss function L , and training data composed of pairs of example inputs and targets (x_i, y_i) . Representing the inputs and targets with random variables x and y , the training procedure finds the parameters that result in the lowest average loss over the training data:

$$\underset{\theta}{\operatorname{argmin}} \mathbb{E}_{x,y} [L(f_{\theta}(x), y)]. \quad (1)$$

As noted by the Noise2Noise authors, this training procedure is equivalent to performing the minimization separately for each input [Lehtinen et al. 2018], so expression (1) becomes

$$\underset{\theta}{\operatorname{argmin}} \mathbb{E}_x [\mathbb{E}_{y|x} [L(f_{\theta}(x), y)]] . \quad (2)$$

The Noise2Noise authors then show that the estimate is the same if the training targets y are replaced with any random variable \hat{y} whose expected value $\mathbb{E}[\hat{y}] = y$ [Lehtinen et al. 2018]. In the denoising scenario, we can therefore replace the clean training targets with noisy ones without changing the result, as long as the noise has zero mean [Lehtinen et al. 2018]. For denoising, the training inputs are also noisy estimates \hat{x} of the clean targets y (not necessarily from the same distribution as the noisy targets \hat{y}), such that $\mathbb{E}[\hat{y} | \hat{x}] = y$ [Lehtinen et al. 2018]. Substituting \hat{x} and \hat{y} into expression (2) results in the Noise2Noise training procedure:

$$\underset{\theta}{\operatorname{argmin}} \mathbb{E}_{\hat{x}} [\mathbb{E}_{\hat{y}|\hat{x}} [L(f_{\theta}(\hat{x}), \hat{y})]] . \quad (3)$$

4 Nonlinear Noise2Noise

4.1 Loss Functions

Since the choice of loss function affects the training results, we start by analyzing the effects of some relevant loss functions on the Noise2Noise training process. As shown in Section 3, the target of the training is the minimum of the expected loss, which can

be minimized separately for each input \hat{x} . Optimizing the model parameters θ is equivalent to optimizing the model output $f_{\theta}(\hat{x})$. So, defining $\tilde{y} = f_{\theta}(\hat{x})$, expression (3) can therefore be minimized by finding the value of \tilde{y} that minimizes the inner expectation:

$$\operatorname{argmin}_{\tilde{y}} \mathbb{E}_{\hat{y}|\hat{x}} [L(\tilde{y}, \hat{y})] . \quad (4)$$

For some loss functions, the value of \tilde{y} that minimizes expression (4) can be found analytically. We first derive the well-known result that the L_2 loss, $L_2(\tilde{y}, \hat{y}) = (\tilde{y} - \hat{y})^2$, has its minimum at the mean, which in our case is the clean target y . This result can be found by setting the partial derivative to zero, and solving for \tilde{y} :

$$\begin{aligned} 0 &= \frac{\partial}{\partial \tilde{y}} \mathbb{E}_{\hat{y}|\hat{x}} [(\tilde{y} - \hat{y})^2] \\ &= \frac{\partial}{\partial \tilde{y}} (\tilde{y}^2 - 2\tilde{y} \mathbb{E}_{\hat{y}|\hat{x}} [\hat{y}] + \mathbb{E}_{\hat{y}|\hat{x}} [\hat{y}^2]) \\ &= 2\tilde{y} - 2 \mathbb{E}_{\hat{y}|\hat{x}} [\hat{y}] \\ \tilde{y} &= \mathbb{E}_{\hat{y}|\hat{x}} [\hat{y}] = y . \end{aligned}$$

We can verify that this critical point is a minimum by looking at the second partial derivative, $\frac{\partial^2}{\partial \tilde{y}^2} \mathbb{E}_{\hat{y}|\hat{x}} [(\tilde{y} - \hat{y})^2] = 2$. This value is strictly greater than zero for all values of \tilde{y} , so the L_2 loss is strictly convex, and y is its single global minimum.

We next derive the minimum for the relative mean squared error (rMSE) loss, $L_{\text{rMSE}} = (\tilde{y} - \hat{y})^2 / (\hat{y} + \epsilon)^2$, which is designed to minimize the effect of outliers in HDR images [Rousselle et al. 2011]. We again set the partial derivative to zero and solve for \tilde{y} :

$$\begin{aligned} 0 &= \frac{\partial}{\partial \tilde{y}} \mathbb{E}_{\hat{y}|\hat{x}} \left[\frac{(\tilde{y} - \hat{y})^2}{(\hat{y} + \epsilon)^2} \right] \\ &= 2\tilde{y} \mathbb{E}_{\hat{y}|\hat{x}} \left[\frac{1}{(\hat{y} + \epsilon)^2} \right] - 2 \mathbb{E}_{\hat{y}|\hat{x}} \left[\frac{\hat{y}}{(\hat{y} + \epsilon)^2} \right] \\ \tilde{y} &= \frac{\mathbb{E}_{\hat{y}|\hat{x}} \left[\frac{\hat{y}}{(\hat{y} + \epsilon)^2} \right]}{\mathbb{E}_{\hat{y}|\hat{x}} \left[\frac{1}{(\hat{y} + \epsilon)^2} \right]} \approx \frac{\mathbb{E}_{\hat{y}|\hat{x}} \left[\frac{1}{\hat{y}^2} \right]}{\mathbb{E}_{\hat{y}|\hat{x}} \left[\frac{1}{(\hat{y} + \epsilon)^2} \right]} . \end{aligned} \quad (5)$$

This value is not easy to simplify because of the nonlinear functions involved, since in general $\mathbb{E}[\varphi(\hat{y})] \neq \varphi(\mathbb{E}[\hat{y}])$. We will show how to analyze this value further in Section 4.3. For now, we can verify that this critical point is a minimum by looking at the first partial derivative above. Our variables represent images and are therefore nonnegative (ignoring negatives from color space transformations or negative filter lobes), so the derivative will be positive when

$$\begin{aligned} 2\tilde{y} \mathbb{E}_{\hat{y}|\hat{x}} \left[\frac{1}{(\hat{y} + \epsilon)^2} \right] &> 2 \mathbb{E}_{\hat{y}|\hat{x}} \left[\frac{\hat{y}}{(\hat{y} + \epsilon)^2} \right] \\ \tilde{y} &> \frac{\mathbb{E}_{\hat{y}|\hat{x}} \left[\frac{\hat{y}}{(\hat{y} + \epsilon)^2} \right]}{\mathbb{E}_{\hat{y}|\hat{x}} \left[\frac{1}{(\hat{y} + \epsilon)^2} \right]} , \end{aligned}$$

which is the value in equation (5). Similarly, the derivative will be zero at this value, and negative when \tilde{y} is less than this value. L_{rMSE} is therefore pseudoconvex for $\tilde{y} \geq 0$, and so the local minimum in equation (5) is also the single global minimum [Mangasarian 1965].

The final loss function we consider is the L_{HDR} loss, $L_{\text{HDR}} = (\tilde{y} - \hat{y})^2 / (\hat{y} + \epsilon)^2$, which is proposed by the Noise2Noise authors as

an alternative to L_{MSE} that avoids the nonlinearity issues [Lehtinen et al. 2018]. Solving the partial derivative again, we have

$$\begin{aligned} 0 &= \frac{\partial}{\partial \tilde{y}} \mathbb{E}_{\hat{y}|\hat{x}} \left[\frac{(\tilde{y} - \hat{y})^2}{(\tilde{y} + \epsilon)^2} \right] \\ &= \frac{2\tilde{y}}{(\tilde{y} + \epsilon)^3} (\mathbb{E}_{\hat{y}|\hat{x}}[\hat{y}] + \epsilon) - \frac{2}{(\tilde{y} + \epsilon)^3} (\mathbb{E}_{\hat{y}|\hat{x}}[\hat{y}^2] + \epsilon \mathbb{E}_{\hat{y}|\hat{x}}[\hat{y}]) \\ \tilde{y} &= \frac{\mathbb{E}_{\hat{y}|\hat{x}}[\hat{y}^2] + \epsilon \mathbb{E}_{\hat{y}|\hat{x}}[\hat{y}]}{\mathbb{E}_{\hat{y}|\hat{x}}[\hat{y}] + \epsilon} \approx \frac{\mathbb{E}_{\hat{y}|\hat{x}}[\hat{y}^2]}{\mathbb{E}_{\hat{y}|\hat{x}}[\hat{y}]} = y + \frac{\text{Var}(\hat{y})}{y}, \end{aligned} \quad (6)$$

where the last equality comes from the definition of variance: $\text{Var}(X) = \mathbb{E}[X^2] - \mathbb{E}[X]^2$. The nonlinearity is easily removed in this case, revealing a bias term of the variance divided by the mean, which is also known as the index of dispersion. We can see that, in the same way as L_{MSE} , the first partial derivative above is negative before the minimum at equation (6), zero at the minimum, and positive after. L_{HDR} is therefore pseudoconvex for $\tilde{y} \geq 0$, and so the local minimum in equation (6) is also the single global minimum [Mangasarian 1965]. Since the denominator can be separated from the expectation, L_{HDR} can also be defined with the gradient of the denominator set to zero, which removes the bias [Lehtinen et al. 2018]. We call this definition L_{HDR}^* , and we evaluate it separately in Section 5.2.

4.2 Loss Functions with Nonlinearity

We now introduce our method, where a nonlinear function $T(v)$ is applied to the model output \tilde{y} and the noisy target \hat{y} before they are passed to the loss function L , which then becomes $L(T(\tilde{y}), T(\hat{y}))$. $T(v)$ must be twice differentiable, strictly monotonic, and nonnegative for $v \geq 0$. In our example application, $T(v)$ is a tone mapping function that reduces the dynamic range of the loss function inputs.

We now analyze the same loss functions as in Section 4.1, but with $T(v)$ applied to their inputs. Starting with the L_2 loss, we have:

$$\begin{aligned} 0 &= \frac{\partial}{\partial \tilde{y}} \mathbb{E}_{\hat{y}|\hat{x}} [(T(\tilde{y}) - T(\hat{y}))^2] \\ &= \frac{\partial}{\partial \tilde{y}} (T(\tilde{y})^2 - 2T(\tilde{y}) \mathbb{E}_{\hat{y}|\hat{x}}[T(\hat{y})] + \mathbb{E}_{\hat{y}|\hat{x}}[T(\hat{y})^2]) \\ &= 2T(\tilde{y})T'(\tilde{y}) - 2T'(\tilde{y}) \mathbb{E}_{\hat{y}|\hat{x}}[T(\hat{y})] \\ \tilde{y} &= T^{-1} (\mathbb{E}_{\hat{y}|\hat{x}}[T(\hat{y})]). \end{aligned} \quad (7)$$

To show that this value is a minimum, we look at the first partial derivative above, which is positive when

$$\begin{aligned} 2T(\tilde{y})T'(\tilde{y}) &> 2T'(\tilde{y}) \mathbb{E}_{\hat{y}|\hat{x}}[T(\hat{y})] \\ \tilde{y} &> T^{-1} (\mathbb{E}_{\hat{y}|\hat{x}}[T(\hat{y})]), \end{aligned}$$

zero at this value, and negative otherwise. For the last line above, the direction of the inequality changes twice if $T(v)$ is strictly decreasing, resulting in no change to the direction. The expected loss is therefore pseudoconvex for $\tilde{y} \geq 0$, and so the local minimum in equation (7) is also the single global minimum [Mangasarian 1965].

The L_{MSE} loss becomes $(T(\tilde{y}) - T(\hat{y}))^2 / (T(\hat{y}) + \epsilon)^2$ with our method, which has its single global minimum at

$$\tilde{y} = T^{-1} \left(\frac{\mathbb{E}_{\hat{y}|\hat{x}} \left[\frac{T(\hat{y})}{(T(\hat{y}) + \epsilon)^2} \right]}{\mathbb{E}_{\hat{y}|\hat{x}} \left[\frac{1}{(T(\hat{y}) + \epsilon)^2} \right]} \right) \approx T^{-1} \left(\frac{\mathbb{E}_{\hat{y}|\hat{x}} \left[\frac{1}{T(\hat{y})} \right]}{\mathbb{E}_{\hat{y}|\hat{x}} \left[\frac{1}{T(\hat{y})^2} \right]} \right), \quad (8)$$

while the L_{HDR} loss becomes $(T(\tilde{y}) - T(\hat{y}))^2 / (T(\hat{y}) + \epsilon)^2$ with our method, which has its single global minimum at

$$\tilde{y} = T^{-1} \left(\frac{\mathbb{E}_{\hat{y}|\hat{x}}[T(\hat{y})^2] + \epsilon \mathbb{E}_{\hat{y}|\hat{x}}[T(\hat{y})]}{\mathbb{E}_{\hat{y}|\hat{x}}[T(\hat{y})] + \epsilon} \right) \approx T^{-1} \left(\frac{\mathbb{E}_{\hat{y}|\hat{x}}[T(\hat{y})^2]}{\mathbb{E}_{\hat{y}|\hat{x}}[T(\hat{y})]} \right), \quad (9)$$

using the same methods as above.

The meaning of these minimum values is not immediately obvious because of the nonlinear functions present inside of the expectations. In the next section, we will show how to derive bounds on the bias introduced by these nonlinearities, and in the following section we will show how to ensure that these bounds are as small as possible.

4.3 Bounding the Jensen Gap

Jensen's inequality states that $\mathbb{E}[\varphi(X)] \geq \varphi(\mathbb{E}[X])$ for a finite random variable X when φ is a convex function [Jensen 1906]. The difference between the two sides of the inequality, $\mathbb{E}[\varphi(X)] - \varphi(\mathbb{E}[X])$, is known as the Jensen gap. We use the method of Liao and Berg [2019] to derive bounds for the Jensen gap, which only requires that φ is twice differentiable (not necessarily convex). With this method, lower and upper bounds for the Jensen gap can be derived with the form $J(\mu) \text{Var}(X)$, where J is a function of the mean μ that is related to the curvature of the nonlinear function φ . Intuitively, the Jensen gap bound will be smaller when φ is closer to being linear, especially around the mean μ . The bound will also be smaller when the variance $\text{Var}(X)$ is smaller, since the random samples will be exposed to less of the nonlinearity of φ . In particular, the Jensen gap bound of Liao and Berg [2019] is

$$J_-(\mu) \text{Var}(X) \leq \mathbb{E}[\varphi(X)] - \varphi(\mathbb{E}[X]) \leq J_+(\mu) \text{Var}(X), \quad (10)$$

where

$$J_-(\mu) = \inf_{x \in (a,b)} h(x, \mu) \text{ and } J_+(\mu) = \sup_{x \in (a,b)} h(x, \mu),$$

and

$$h(x, \mu) = \frac{\varphi(x) - \varphi(\mu)}{(x - \mu)^2} - \frac{\varphi'(\mu)}{x - \mu}.$$

In our case, we have $a = 0$, $b = \infty$, $X = \hat{y}$, and $\mu = y$. Note that the variance identity applied in equation (6) is a special case of inequality (10), where $J_- = J_+ = 1$ for $\varphi(X) = X^2$. Note as well that it is possible to derive tighter bounds on the Jensen gap using higher central moments than $\text{Var}(X)$ [Lee et al. 2021], but these moments are less interpretable for arbitrary distributions.

We now apply the method of Liao and Berg [2019] to the minimum expected loss values derived in Section 4.2. Starting with the $L_2(T(\tilde{y}), T(\hat{y}))$ loss, the nonlinearity in equation (7) is $T(\hat{y})$. We therefore set $\varphi(X) = T(\hat{y})$ in inequality (10), giving

$$\begin{aligned} J_-(y) \text{Var}(\hat{y}) &\leq \mathbb{E}[T(\hat{y})] - T(\mathbb{E}[\hat{y}]) \leq J_+(y) \text{Var}(\hat{y}) \\ T(y) + J_-(y) \text{Var}(\hat{y}) &\leq \mathbb{E}[T(\hat{y})] \leq T(y) + J_+(y) \text{Var}(\hat{y}) \\ T^{-1}(T(y) + J_-(y) \text{Var}(\hat{y})) &\leq \tilde{y} \leq T^{-1}(T(y) + J_+(y) \text{Var}(\hat{y})), \end{aligned}$$

where in the last line we have applied equation (7). Note that both inequalities change direction in the last line if $T(v)$ is strictly decreasing. Intuitively, we have bias terms of the form $J(y) \text{Var}(\hat{y})$ that are applied in the nonlinear space defined by $T(v)$, and then the

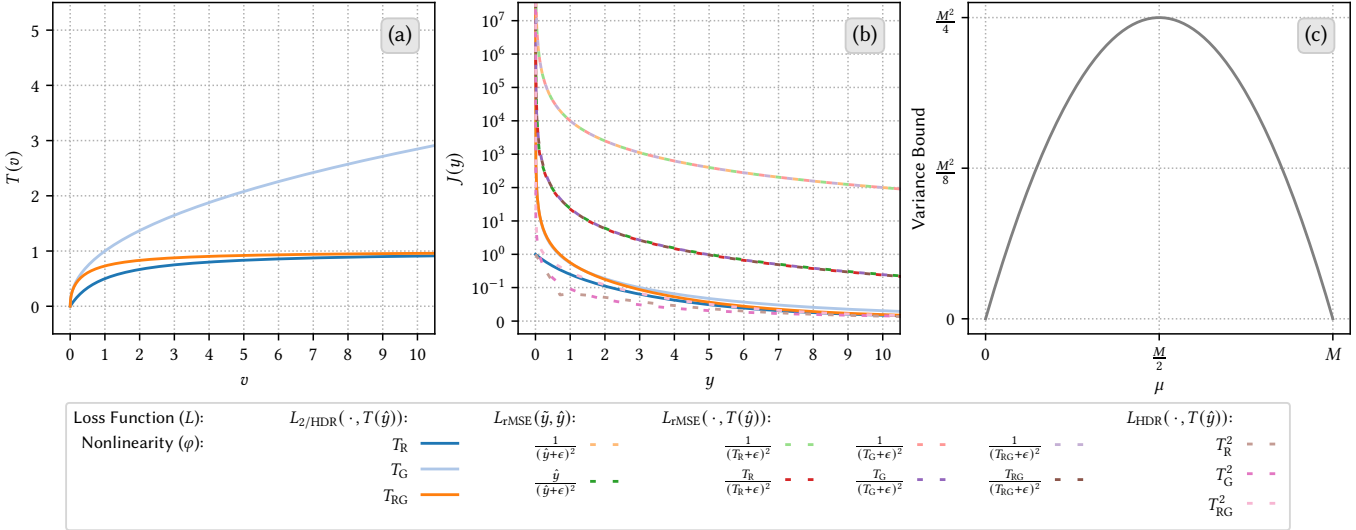


Fig. 2. (a) Tone mapping functions used for our experimental results. See Section 5.2 for details. (b) $J(y)$ functions for the listed $\varphi(\hat{y})$ functions resulting from all combinations of our studied loss functions and tone mapping functions. $J_-(y)$ and $J_+(y)$ functions are represented together as $\max(|J_-(y)|, |J_+(y)|)$, with $\epsilon = 0.01$. See Section 4.3 for details on $J(y)$ functions, and Section A.1 for a list of the $J(y)$ functions plotted above. (c) Graphical representation of the Bhatia-Davis inequality for bounded probability distributions with minimum $m = 0$ and maximum M . See Section 4.4 for details.

results are mapped back to the linear space by $T^{-1}(v)$. We assume that the J_- terms do not make the resulting values negative.

For the $L_{\text{tMSE}}(T(\hat{y}), T(\hat{y}))$ loss, we apply the same procedure as above to equation (8) to obtain an upper bound of

$$\tilde{y} \leq T^{-1} \left(\frac{\frac{T(y)}{(T(y)+\epsilon)^2} + J_+^{-1}(y) \text{Var}(\hat{y})}{\frac{1}{(T(y)+\epsilon)^2} + J_-^{-2}(y) \text{Var}(\hat{y})} \right),$$

where again the inequality changes direction if $T(v)$ is strictly decreasing (making this the lower bound). To obtain the other bound, change the direction of the inequality, and swap the subscripts of the $J(y)$ functions. Here, $J_{+/-}^{-1}(y)$ and $J_{+/-}^{-2}(y)$ mean the $J_{+/-}(y)$ functions for $\varphi(\hat{y}) = \frac{T(\hat{y})}{(T(\hat{y})+\epsilon)^2}$ and $\varphi(\hat{y}) = \frac{1}{(T(\hat{y})+\epsilon)^2}$, respectively.

For the $L_{\text{HDR}}(T(\hat{y}), T(\hat{y}))$ loss, we apply the same procedure to equation (9) to obtain an upper bound of

$$\tilde{y} \leq T^{-1} \left(\frac{T(y)^2 + J_+^2(y) \text{Var}(\hat{y}) + \epsilon(T(y) + J_+(y) \text{Var}(\hat{y}))}{T(y) + J_-(y) \text{Var}(\hat{y}) + \epsilon} \right),$$

where again the inequality changes direction if $T(v)$ is strictly decreasing (making this the lower bound). To obtain the other bound, change the direction of the inequality, and swap the subscripts of the $J(y)$ functions. Here, $J_{+/-}^2(y)$ and $J_{+/-}(y)$ mean the $J_{+/-}(y)$ functions for $\varphi(\hat{y}) = T(\hat{y})^2$ and $\varphi(\hat{y}) = T(\hat{y})$, respectively.

We can also now derive the Jensen gap bound for the original $L_{\text{tMSE}}(\tilde{y}, \hat{y})$ loss, as promised in Section 4.1. Applying the same procedure as above to equation (5), we obtain a bound of

$$\frac{\frac{y}{(y+\epsilon)^2} + J_-^{-1}(y) \text{Var}(\hat{y})}{\frac{1}{(y+\epsilon)^2} + J_+^{-2}(y) \text{Var}(\hat{y})} \leq \tilde{y} \leq \frac{\frac{y}{(y+\epsilon)^2} + J_+^{-1}(y) \text{Var}(\hat{y})}{\frac{1}{(y+\epsilon)^2} + J_-^{-2}(y) \text{Var}(\hat{y})},$$

where $J_{+/-}^{-1}(y)$ and $J_{+/-}^{-2}(y)$ mean the $J_{+/-}(y)$ functions for $\varphi(\hat{y}) = \frac{\hat{y}}{(\hat{y}+\epsilon)^2}$ and $\varphi(\hat{y}) = \frac{1}{(\hat{y}+\epsilon)^2}$, respectively.

The $J(y)$ functions for the tone mapping functions we evaluate in our experiments (see Section 5.2) are plotted in Figure 2(b), and are listed in Section A.1.

4.4 Minimizing the Jensen Gap

In Section 4.3 we showed how to derive Jensen gap bounds for nonlinear functions applied to some relevant loss functions. We now show how to ensure that these bounds are as small as possible. There are two cases where the bounds derived above are small, namely when $\text{Var}(\hat{y})$ is small, or when $\varphi(\hat{y})$ is nearly linear [Liao and Berg 2019]. The first case, where $\text{Var}(\hat{y})$ is small, can be difficult to achieve in practice. For applications like long-exposure photography or Monte Carlo rendering, the noise is gradually reduced over time, and zero noise is only reached after an infinite amount of time. Since we only have a finite amount of time in practice, there will always be some amount of noise remaining, even in the so-called “clean” target images. So, in a sense, we are always doing Noise2Noise training in these situations, even when training with “clean” targets [Tintis 2022]. Therefore, the Jensen gap bound is a concern even with “clean” targets, although the effect will be larger when the targets have a significant amount of noise.

The other case where the Jensen gap is small is when $\varphi(\hat{y})$ is nearly linear. This is acceptable when nonlinear functions are not needed, but there are practical applications where nonlinear functions are useful. Dynamic range reduction, for example, is not possible with a linear function, yet significantly improves the stability of the training process. It is therefore advisable to choose nonlinear functions that both have practical benefits, and also have low Jensen

gap bounds. For example, the tone mapping functions that we use for our experimental results are plotted in Figure 2(a). For effective dynamic range reduction, the function should have more curvature near zero, and less towards infinity. This property also results in low $J(y)$ values for most of the function domain, except near zero (see the solid lines in Figure 2(b)). HDR images will therefore often have low $J(y)$ values for these tone mapping functions, since the clean targets y will often have large values.

There is also a separate reason for why the Jensen gap bound will be small when the clean target y is small. For most practical purposes, y will in fact have a maximum possible value M . This value could come from the maximum representable value of the data format, the maximum possible output value of the camera sensor, or the maximum brightness of the light sources in a rendered scene, for example. Given this maximum value M , the Bhatia-Davis inequality lets us bound the variance $\text{Var}(\hat{y})$ to

$$\text{Var}(\hat{y}) \leq (M - y)(y - m) = -y^2 + My,$$

for the minimum value $m = 0$ [Bhatia and Davis 2000]. This bound forms a parabola with roots at $y = 0$ and $y = M$, and a maximum value of $\frac{M^2}{4}$ at $y = \frac{M}{2}$ (see Figure 2(c)). This maximum value is also known as Popoviciu's inequality [Popoviciu 1935]. Because of the roots of the parabola, this bound on the variance will be small for y values near $y = 0$ and $y = M$.

In summary, for a low Jensen gap bound, choose a nonlinear function with low curvature, especially near where the clean targets will be located. For bounded probability distributions, the function can have some curvature near the minimum and maximum possible values. In the next section, we present our experimental results, and show that the practical benefits of certain nonlinear functions can vastly outweigh the bias that they introduce to the results.

5 Experimental Results

We demonstrate the effectiveness of our method by applying it to a Monte Carlo denoising task. We first describe our experimental methods (Section 5.1), then we evaluate several combinations of loss functions and tone mapping functions (Section 5.2), and then we compare our method to training with clean references (Section 5.3).

5.1 Methods

We apply our training method to an offline Monte Carlo denoising algorithm called Sample-Based Monte Carlo Denoising (SBMC) [Gharbi et al. 2019]. We chose SBMC as our denoiser because of its adaptability to various simple loss functions, and because of its publicly available test set for comparisons [Gharbi et al. 2019]. Our aim was to reproduce the denoising results of the SBMC authors, but using Noise2Noise training instead of the clean reference images used by the original implementation. This process involved generating randomized scenes for training, rendering these scenes to noisy image pairs with additional feature data, training SBMC models for various combinations of loss functions and tone mapping functions, and evaluating their denoising performance.

Scene generation. The training scenes are randomly generated to include a wide variety of objects, materials, and light transport scenarios. This variety ensures that the resulting denoising models

can handle a diverse range of scenes. We used the scene generator from SBMC [Gharbi et al. 2019], which generates both indoor and outdoor scenes. For indoor scenes, it uses a dataset of room models called SunCG [Song et al. 2017], which is no longer available [Robitzski 2019], so our dataset consists of only outdoor scenes. We did not substitute another dataset for indoor scenes to avoid any factors that could artificially improve our performance relative to SBMC. This difference could affect the ability of our models to generalize to indoor scenes, and should be taken into account when comparing the performance of our models to SBMC.

Rendering. We used the PBRT v2 renderer [Pharr et al. 2023] with the patch provided by SBMC to save the Monte Carlo samples separately and to gather additional feature data [Gharbi et al. 2019]. We implemented Noise2Noise training by rendering two different noisy images for each scene, each with different random seeds. One pair of noisy images is rendered for each generated scene to maximize the diversity of the training dataset.

Dataset. Our goal in generating a training dataset was to match the dataset used by SBMC, to allow for testing our method without changing any other variables. To match SBMC, we generated a training dataset of around 300,000 example pairs at 128×128 resolution [Gharbi et al. 2019]. The exact number was 283,831 example pairs due to the rejection sampling of the SBMC scene generator. For SBMC, the noisy inputs were rendered at 8 spp and the references were rendered at 4096 spp [Gharbi et al. 2019]. For our training set, the noisy images were both rendered at 8 spp. We also generated a second training set by repeating this process with a different starting seed, resulting in an additional 284,016 example pairs. To monitor progress during training, we also generated a validation set. To match SBMC, our validation set contained around 1000 example pairs with references rendered at 4096 spp [Gharbi et al. 2019], resulting in 937 example pairs after rejection sampling.

Training. We trained our models in the same way as SBMC, with one small modification to improve performance. As with SBMC, the number of input spp was selected randomly from 2 to 8 during training as a form of data augmentation, so that the models can handle different numbers of input spp [Gharbi et al. 2019]. With SBMC this choice is made per training example, while in our implementation the choice is made per training batch. This change allows for greater parallelism, and therefore improved training performance. SBMC has a fixed batch size of one because of this limitation, whereas with our implementation the batch size can be larger and split over multiple graphics processing units (GPUs). Convergence should not be affected since the model is still exposed to a variety of spp. In particular, we use a batch size of 16 split over four Nvidia Tesla T4 GPUs with 16 GB of memory each.

5.2 Model Selection

For some applications of nonlinear Noise2Noise, it might be necessary to apply our theoretical analysis to design new nonlinear functions. However, this is not needed for Monte Carlo denoising, since certain combinations of existing loss functions and tone mapping functions meet our theoretical criteria and perform well in practice. Note that there is no universally optimal combination of

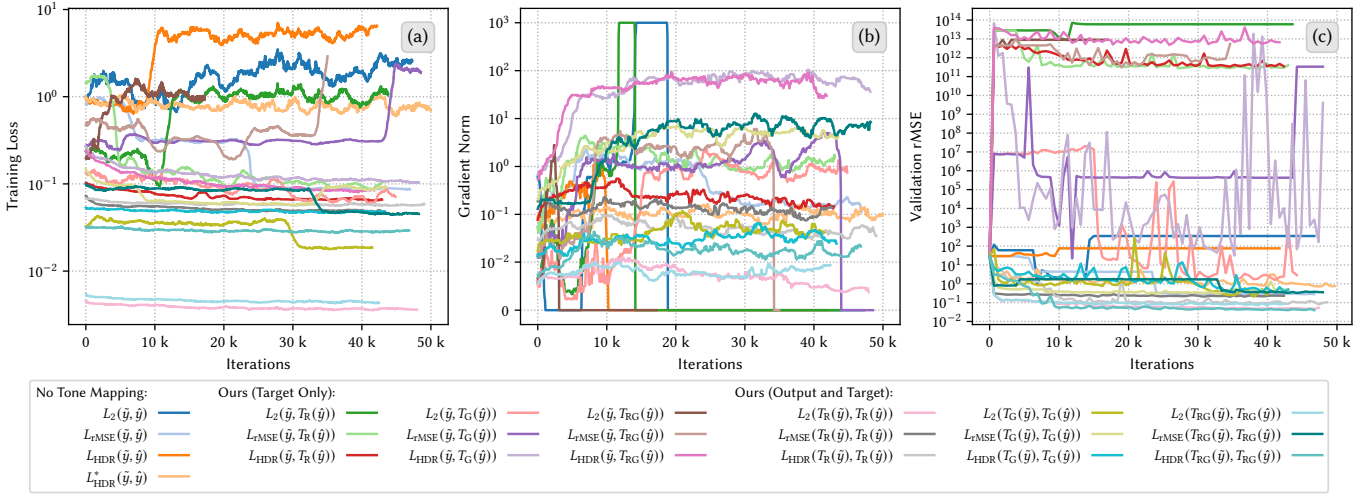


Fig. 3. (a) Training losses, (b) Gradient norms, and (c) Validation rMSE for all combinations of loss functions, tone mapping functions, and tone mapping placement. For the training losses, the units differ for the different loss functions, so comparisons in terms of loss value are not meaningful, and instead we are interested in the numerical stability of the loss landscapes. The training losses and gradient norms are smoothed with a centered median filter with a width of 2,000 iterations. The gradient norms were clipped at a value of 10^3 during training, and so will not exceed this value. Training runs that end before 40,000 iterations were terminated due to numerical errors.

loss function and tone mapping function, because the performance depends on the denoising model and data distribution. Therefore, we choose the combination with the best experimental performance on our model and dataset.

We consider the loss functions introduced in Section 4.1, which correspond to the losses used by SBMC and Noise2Noise [Gharbi et al. 2019; Lehtinen et al. 2018]. The plain L_2 loss without tone mapping is unbiased, but is easily affected by outliers, so we do not expect it to perform well in practice. The L_{TMSE} and L_{HDR} losses are normalized to reduce the impact of outliers. However, our theoretical results show that the plain L_{TMSE} and L_{HDR} losses have relatively high Jensen gap bounds (see Figure 2(b); L_{HDR} has a constant $J(y) = 1$), so we do not expect strong performance from these losses. L_{HDR}^* , on the other hand, is both normalized and unbiased, and could therefore perform well if the normalization is effective.

We consider several common tone mapping functions, including Reinhard's function, $T_R(v) = v/(1+v)$ [Reinhard et al. 2010], which is used by SBMC [Gharbi et al. 2019], and a variant used by Noise2Noise that adds gamma compression, $T_{RG}(v) = (v/(1+v))^{1/2.2}$ [Lehtinen et al. 2018]. Gamma compression alone, $T_G(v) = v^{1/2.2}$, is also a common tone mapping function, so we have included it in our comparisons. These tone mapping functions, when combined with the L_2 or L_{HDR} losses, match the theoretical requirements described in Section 4.4 (again see Figure 2(b)), and so would be expected to perform well. The tone mapping functions combined with the L_{TMSE} loss have relatively high Jensen gap bounds, and so would not be expected to perform well.

We consider three options of where to apply tone mapping: to both the model output and the target image, to only the target image, or to neither. Tone mapping only the target image is an alternative version of our method that can be interpreted as asking the model

to generate outputs in the tone mapped scale. We convert these tone mapped outputs back to the linear scale with the inverse tone mapping function for evaluation. We do not consider applying tone mapping to only the model output as this would be nonsensical. This scenario would require the model to generate huge values that would then be tone mapped down to reach the already large HDR values in the target images. SBMC and Noise2Noise both find that tone mapping the model input \hat{x} is beneficial as well [Gharbi et al. 2019; Lehtinen et al. 2018], so we follow that practice. SBMC uses a separate tone mapping function for the model input, $T_i(v) = \frac{1}{10} \ln(1+v)$, which we keep in place for all of our experiments.

Evaluating all of the possible combinations of three loss functions, three tone mapping functions, and three options of where to apply them, would require a grid search with 27 entries. However, some of the entries are redundant: there is no need to try the different tone mapping functions when tone mapping is not used. This reduces the number of trials to 21. We also add a trial for the $L_{HDR}^*(\hat{y}, \hat{y})$ variant, bringing the total number of trials to 22. It is not necessary to combine L_{HDR}^* with tone mapping, since the bias in that case would be the same as that of L_2 with tone mapping, which we already evaluate. We trained an SBMC model using each of these configurations, with all other parameters remaining the same. The non-tone mapped rMSE loss was calculated for validation regardless of which loss function and tone mapping function were used for training. The training losses, gradient norms, and validation losses for each model are shown in Figure 3. The output of each model on a single validation image is shown in Figure 4, with additional validation images shown in Section A.3.

As predicted, the plain L_2 , L_{TMSE} , and L_{HDR} loss functions do not perform well. L_{HDR}^* also performs poorly, indicating that it does not have sufficient outlier rejection. In Figure 3(a), these loss functions

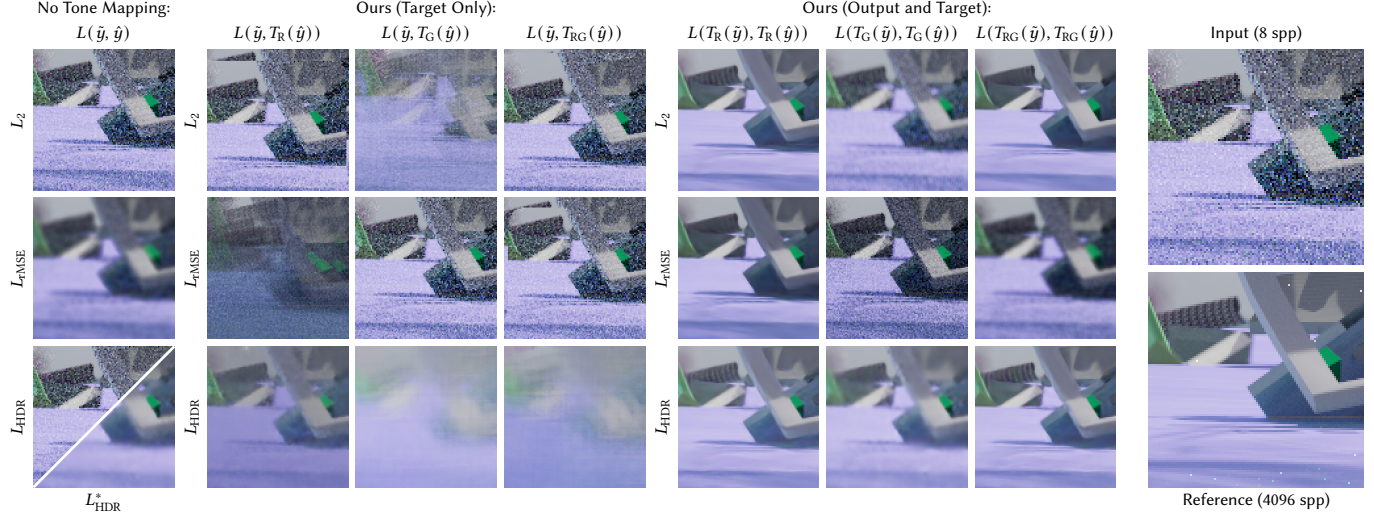


Fig. 4. Model outputs for a single validation image for all combinations of loss functions, tone mapping functions, and tone mapping placement

all show large and noisy training loss values. Note that since the training losses have different units, we cannot compare the loss values directly. Instead, we are interested in the numerical stability of the loss landscapes. In Figure 3(b), we can see that these unstable loss functions lead to exploding and vanishing gradients in the case of $L_2(\tilde{y}, \hat{y})$ and $L_{\text{HDR}}(\tilde{y}, \hat{y})$, causing the training process to stall. This stalled training can be seen in Figure 3(c), where the validation losses fail to converge. $L_{\text{rMSE}}(\tilde{y}, \hat{y})$ and $L_{\text{HDR}}^*(\tilde{y}, \hat{y})$ show better stability in Figure 3(b), but have large validation loss values in Figure 3(c). The plain loss functions also perform poorly in Figure 4, where the validation images are either overly noisy or blurry.

Turning to our method, the loss functions with tone mapping of the model output and target image mostly perform well, as predicted. $L_2(T(\tilde{y}), T(\hat{y}))$ and $L_{\text{HDR}}(T(\tilde{y}), T(\hat{y}))$ have low and smooth training losses and gradient norms in Figures 3(a) and 3(b) for all of the tone mapping functions. These losses also show good denoising performance in Figures 3(c) and 4, with the exception of the T_G tone mapping function. T_R and T_{RG} both perform well here, which indicates that their differing $J(y)$ values for low values of y (see Figure 2(b)) are not important. This observation supports the idea that the variance bound (see Figure 2(c)) is dominant for low y . The poor performance of T_G here, despite having similar $J(y)$ curves to the other tone mapping functions, could be because of the difference shown in Figure 2(a), where T_G has unbounded output values. The $L_{\text{rMSE}}(T(\tilde{y}), T(\hat{y}))$ losses perform poorly, as predicted by their large $J(y)$ values. The loss functions with tone mapping applied to only the target image also perform poorly, with large and noisy training losses and gradients, and poor denoising results. The lowest validation loss overall is achieved by $L_{\text{HDR}}(T_{RG}(\tilde{y}), T_{RG}(\hat{y}))$. This loss function also has the best qualitative denoising result, with more detail preserved in the background objects.

5.3 Comparing to Clean References

We now compare our nonlinear Noise2Noise method to training with clean reference images. Training with clean references is represented by the original SBMC implementation [Gharbi et al. 2019], and our method is represented by the best performing combination of loss function and tone mapping function from Section 5.2. We did not include the models with plain loss functions or tone mapping of only the target image in this comparison, because none of these models produced acceptable denoising results. We trained our model again for seven days to allow for any performance improvements that could occur over longer training times. We also trained another model with the same configuration for seven days on a dataset of twice the size composed of our original training set combined with our additional training set. The two datasets were shuffled together so that the model was exposed to examples from both datasets at random. Extending the training time to seven days resulted in slightly lower validation loss values for both models. Training with the larger dataset did not result in a significant improvement in validation loss compared with training on the original dataset.

We performed our comparisons using the SBMC test set, which consists of 55 scenes collected from publicly available sources [Gharbi et al. 2019]. The SBMC authors provide reference images for each scene rendered at 1024×1024 resolution with 8192 spp [Gharbi et al. 2019]. The low-sample count input images with additional feature data are not provided, so we rendered these using the provided scene files. The SBMC authors compare their work against five other denoisers [Bako et al. 2017; Bitterli et al. 2016; Kalantari et al. 2015; Rousselle et al. 2012; Sen and Darabi 2012]. We include error numbers for SBMC and the other denoisers using the data from Table 1 of the SBMC paper [Gharbi et al. 2019]. Comparing our models to the other denoisers in this way is fair, since our only changes to the SBMC training set are the lack of indoor scenes, and rendering the references at 8 spp instead of 4096 spp (see Section 5.1). These changes would only serve to disadvantage

Table 1. Error metrics for each denoiser averaged over the SBMC test set (**bold** indicates best result, *italics* indicates second best result)

| | | Input | Ours (Orig.) | Ours (Large) | SBMC | Bako | Bako (f.t.) | Bitterli | Kalantari | Rousselle | Sen |
|---------|-------|---------|---------------|---------------|---------------|---------------|---------------|----------|---------------|-----------|--------|
| 4 spp | rMSE | 17.3054 | 0.8619 | 0.6130 | 0.0482 | 1.0867 | <i>0.4932</i> | 1.0847 | 1.5814 | 2.0416 | 1.0352 |
| | DSSIM | 0.4648 | 0.0815 | 0.0819 | 0.0685 | 0.1294 | 0.1173 | 0.1014 | 0.0869 | 0.1575 | 0.1009 |
| 8 spp | rMSE | 7.4732 | 0.3193 | 0.2940 | 0.0382 | 8.1238 | 0.8471 | 0.9149 | 1.6684 | 2.0721 | 0.5670 |
| | DSSIM | 0.3995 | 0.0707 | 0.0700 | 0.0599 | 0.1190 | 0.0940 | 0.0818 | 0.0708 | 0.1175 | 0.0987 |
| 16 spp | rMSE | 11.0416 | 0.1393 | 0.1052 | 0.0315 | 21.3297 | 0.2934 | 0.9488 | 1.8151 | 2.0481 | 0.3348 |
| | DSSIM | 0.3373 | 0.0623 | 0.0606 | 0.0542 | 0.1128 | 0.0762 | 0.0700 | 0.0600 | 0.0898 | 0.0986 |
| 32 spp | rMSE | 16.5478 | 0.0841 | 0.0588 | 0.0274 | 31.4400 | 0.1427 | 1.1344 | 1.7398 | 1.6447 | 0.2731 |
| | DSSIM | 0.2775 | 0.0572 | 0.0545 | 0.0510 | 0.1106 | 0.0619 | 0.0630 | 0.0516 | 0.0685 | 0.1005 |
| 64 spp | rMSE | 12.0608 | 0.0601 | 0.0437 | 0.0261 | 0.1359 | 0.1553 | 0.8747 | 1.6228 | 1.6974 | – |
| | DSSIM | 0.2223 | 0.0547 | 0.0514 | 0.0494 | 0.0407 | 0.0536 | 0.0566 | 0.0393 | 0.0547 | – |
| 128 spp | rMSE | 1.7717 | 0.0497 | 0.0377 | 0.0254 | 0.0757 | 0.1229 | 0.9039 | 1.7394 | 1.8176 | – |
| | DSSIM | 0.0488 | 0.0539 | 0.0505 | 0.0488 | 0.0353 | 0.0432 | 0.0565 | 0.0414 | 0.0466 | – |

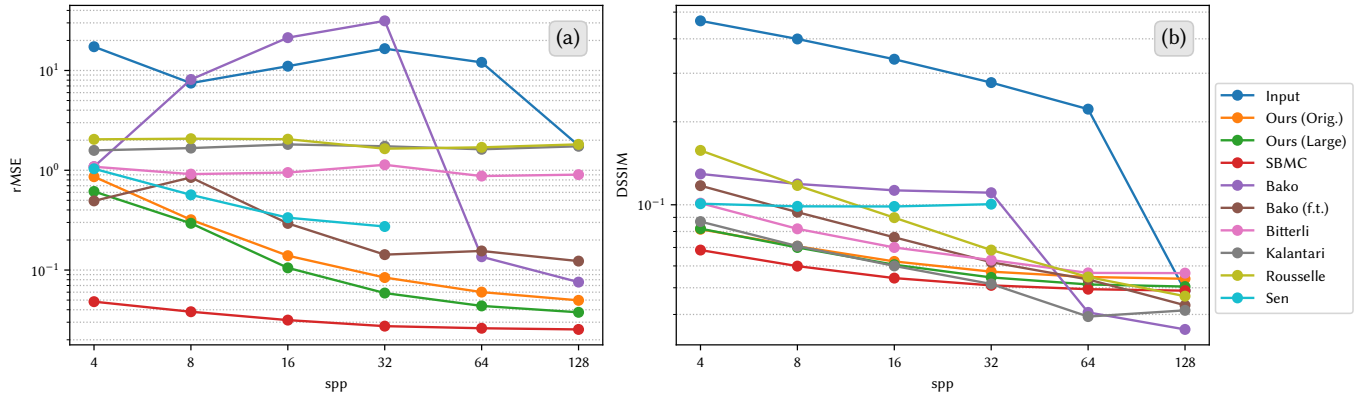


Fig. 5. (a) rMSE and (b) DSSIM error metrics for each denoiser at various input samples per pixel (spp), averaged over the SBMC test set

our models relative to SBMC and the other denoisers. Two error metrics are used for comparison: rMSE, and structural dissimilarity index $DSSIM = 1 - SSIM$ [Wang et al. 2004]. Both of these metrics are used without tone mapping, and are computed so that lower values are better. The results are shown in Table 1 and Figure 5. Some example outputs from our models and SBMC are shown in Figure 1 and Section A.3. Outputs from the other denoisers are in the SBMC supplemental data [Gharbi et al. 2019].

Table 1 and Figure 5 show that the original SBMC implementation achieved the best rMSE results for each of the input sample counts. SBMC also achieved the best DSSIM results for the lower sample counts, with some of the other denoisers taking the lead at higher sample counts. Both of our models produced results that are close to SBMC for all sample counts in terms of DSSIM. The results are close for rMSE at higher sample counts, and about an order of magnitude larger at lower sample counts. Our model trained on the larger dataset performed better than our original model in all cases but one. This difference from the validation results can be explained by the validation and test sets coming from different distributions. Training with even more noisy data is a promising direction for future work. In fact, the Noise2Noise authors were able to surpass the performance of training with clean references for

a different denoising task [Lehtinen et al. 2018]. Compared to the other denoising methods, our models came in second after SBMC in the majority of cases where SBMC had the best performance. This performance was achieved despite our models being trained only on outdoor scenes (see Section 5.1) while being evaluated on a test set that includes many indoor scenes. Figure 1 shows outputs from our models and SBMC on a single test scene. Our models compare well to SBMC, with all three models reducing the rMSE of the noisy input to a single-digit percentage of its original value. In this case, our model trained on the original dataset slightly outperforms our model trained on the larger dataset.

6 Limitations and Conclusions

In this work, we showed that nonlinear functions can be effectively applied to the noisy target images in Noise2Noise training. We presented a theoretical framework for deriving bounds on the bias introduced by this method, and demonstrated that the bias can be negligible compared to the practical benefits. To summarize: choose nonlinear functions with low curvature near the clean target locations. For bounded distributions, some curvature is allowable near the minimum and maximum values. The main limitation of our theoretical approach is that characterizing the Jensen gap bound

analytically is only possible for simple loss functions and nonlinear functions. However, if the bound is not tractable analytically, it may still be possible to evaluate numerically or experimentally. We look forward to future works that demonstrate more applications of our nonlinear Noise2Noise method.

We demonstrated our method on the denoising of Monte Carlo rendered images. We applied our theoretical framework to show that certain combinations of loss functions and tone mapping functions can reduce the effect of outliers while introducing minimal bias to the results. Our nonlinear Noise2Noise method makes it possible to train complex Monte Carlo denoising models for varied scenes from only noisy training data. Our denoising results approach those of the original implementation trained with clean reference images, but our models are trained on $512 \times$ fewer reference samples. We hope that future works will further improve the performance of our nonlinear method by training with even more noisy data, possibly even exceeding the performance of training with clean references.

Acknowledgments

Thank you to Morgan McGuire, Yuri Boykov, and the anonymous reviewers for their helpful comments.

This research was funded in part by NSERC (the Natural Sciences and Engineering Research Council of Canada), the University of Waterloo, and David R. Cheriton. Computing resources for this research were provided in part by Compute Ontario and the Digital Research Alliance of Canada.

References

Jonghee Back, Binh-Son Hua, Toshiya Hachisuka, and Bochang Moon. 2020. Deep combiner for independent and correlated pixel estimates. *ACM Transactions on Graphics* 39, 6 (Nov. 2020), 242:1–242:12. doi:10.1145/3414685.3417847

Jonghee Back, Binh-Son Hua, Toshiya Hachisuka, and Bochang Moon. 2022. Self-Supervised Post-Correction for Monte Carlo Denoising. In *ACM SIGGRAPH 2022 Conference Proceedings (SIGGRAPH '22)*. Association for Computing Machinery, New York, NY, USA, 1–8. doi:10.1145/3528233.3530730

Steve Bako, Thijs Vogels, Brian McWilliams, Mark Meyer, Jan Novák, Alex Harvill, Pradeep Sen, Tony DeRose, and Fabrice Rousselle. 2017. Kernel-Predicting Convolutional Networks for Denoising Monte Carlo Renderings. *ACM Transactions on Graphics (Proceedings of SIGGRAPH 2017)* 36, 4 (July 2017). doi:10.1145/3072959.3073708

Joshua D. Batson and Loïc A. Royer. 2019. Noise2Self: Blind Denoising by Self-Supervision. *ICML* (2019). <http://proceedings.mlr.press/v97/batson19a.html>

Rajendra Bhatia and Chandler Davis. 2000. A Better Bound on the Variance. *The American Mathematical Monthly* 107, 4 (April 2000), 353–357. doi:10.1080/00029890.2000.12005203 Publisher: Taylor & Francis.

Benedikt Bitterli, Fabrice Rousselle, Bochang Moon, José A. Iglesias-Guitián, David Adler, Kenny Mitchell, Wojciech Jarosz, and Jan Novák. 2016. Nonlinearly Weighted First-order Regression for Denoising Monte Carlo Renderings. *Computer Graphics Forum* 35, 4 (July 2016), 107–117. doi:10.1111/cgf.12954

Ashish Bora, Eric Price, and Alexandros G. Dimakis. 2018. AmbientGAN: Generative models from lossy measurements. In *ICLR*. <https://openreview.net/forum?id=Hy7fDogb>

Antoni Buades, Bartomeu Coll, and Jean-Michel Morel. 2005. A non-local algorithm for image denoising. In *2005 IEEE Computer Society Conference on Computer Vision and Pattern Recognition (CVPR'05)*, Vol. 2. IEEE, 60–65. doi:10.1109/CVPR.2005.38

Chakravarty R, Alla Chaitanya, Anton S. Kaplanyan, Christoph Schied, Marco Salvini, Aaron Lefohn, Derek Nowrouzezahrai, and Timo Aila. 2017. Interactive reconstruction of Monte Carlo image sequences using a recurrent denoising autoencoder. *ACM Transactions on Graphics (TOG)* 36, 4 (2017), 98. doi:10.1145/3072959.3073601

Bingyi Chen, Zengyu Liu, Li Yuan, Zhifan Liu, Yi Li, Guan Wang, and Ning Xie. 2023. Monte Carlo Denoising via Multi-scale Auxiliary Feature Fusion Guided Transformer. In *SIGGRAPH Asia 2023 Technical Communications (SA '23)*. Association for Computing Machinery, New York, NY, USA, 1–4. doi:10.1145/3610543.3626179

Chuhao Chen, Yuze He, and Tzu-Mao Li. 2024. Temporally Stable Metropolis Light Transport Denoising using Recurrent Transformer Blocks. *ACM Trans. Graph.* 43, 4 (July 2024), 123:1–123:14. doi:10.1145/3658218

In-Young Cho, Yuchi Huo, and Sung-Eui Yoon. 2021. Weakly-supervised contrastive learning in path manifold for Monte Carlo image reconstruction. *ACM Transactions on Graphics* 40, 4 (July 2021), 38:1–38:14. doi:10.1145/3450626.3459876

Hajin Choi, Seokpyo Hong, Inwoo Ha, Nahyup Kang, and Bochang Moon. 2024. Online Neural Denoising with Cross-Regression for Interactive Rendering. *ACM Trans. Graph.* 43, 6 (Nov. 2024), 221:1–221:12. doi:10.1145/3687938

Kostadin Dabov, Alessandro Foi, Vladimir Katkovnik, and Karen Egiazarian. 2007. Image Denoising by Sparse 3-D Transform-Domain Collaborative Filtering. *IEEE Transactions on Image Processing* 16, 8 (Aug. 2007), 2080–2095. doi:10.1109/TIP.2007.901238

Michaël Gharbi, Tzu-Mao Li, Miika Aittala, Jaakko Lehtinen, and Frédéric Durand. 2019. Sample-based Monte Carlo Denoising Using a Kernel-splatting Network. *ACM Trans. Graph.* 38, 4 (July 2019), 125:1–125:12. doi:10.1145/3306346.3322954

Jie Guo, Mengtian Li, Quewei Li, Yuting Qiang, Bingyang Hu, Yanwen Guo, and Ling-Qi Yan. 2019. GradNet: unsupervised deep screened poisson reconstruction for gradient-domain rendering. *ACM Transactions on Graphics* 38, 6 (Nov. 2019), 223:1–223:13. doi:10.1145/3355089.3356538

Yuchi Huo and Sung-eui Yoon. 2021. A survey on deep learning-based Monte Carlo denoising. *Computational Visual Media* 7, 2 (June 2021), 169–185. doi:10.1007/s41095-021-0209-9

J. L. W. V. Jensen. 1906. Sur les fonctions convexes et les inégalités entre les valeurs moyennes. *Acta Mathematica* 30 (Jan. 1906), 175–193. doi:10.1007/BF02418571 Publisher: Institut Mittag-Leffler.

Nima Khademi Kalantari, Steve Bako, and Pradeep Sen. 2015. A Machine Learning Approach for Filtering Monte Carlo Noise. *ACM Trans. Graph.* 34, 4 (July 2015), 122:1–122:12. doi:10.1145/2766977

Alexander Krull, Tim-Oliver Buchholz, and Florian Jug. 2019. Noise2Void - Learning Denoising From Single Noisy Images. In *Proceedings of the IEEE/CVF Conference on Computer Vision and Pattern Recognition (CVPR)*, 2129–2137. doi:10.1109/CVPR.2019.00223

Samuli Laine, Tero Karras, Jaakko Lehtinen, and Timo Aila. 2019. High-Quality Self-Supervised Deep Image Denoising. In *Advances in Neural Information Processing Systems 32 (NeurIPS 2019)*, Vol. 32, 6970–6980. <https://proceedings.neurips.cc/paper/2019/hash/2119b8d43eacf353e07d7cb5554170b-Abstract.html>

Sang Kyu Lee, Jae Ho Chang, and Hyoung-Moon Kim. 2021. Further sharpening of Jensen's inequality. *Statistics* 55, 5 (Sept. 2021), 1154–1168. doi:10.1080/02331888.2021.1998052

Jaakko Lehtinen, Jacob Munkberg, Jon Hasselgren, Samuli Laine, Tero Karras, Miika Aittala, and Timo Aila. 2018. Noise2Noise: Learning Image Restoration without Clean Data. In *International Conference on Machine Learning*. PMLR, 2965–2974. <http://proceedings.mlr.press/v80/lehtinen18a.html>

J. G. Liao and Arthur Berg. 2019. Sharpening Jensen's Inequality. *The American Statistician* 73, 3 (July 2019), 278–281. doi:10.1080/00031305.2017.1419145 Publisher: American Statistical Association.

Weiheng Lin, Beibei Wang, Lu Wang, and Nicolas Holzschuch. 2020. A Detail Preserving Neural Network Model for Monte Carlo Denoising. *Computational Visual Media* 6 (April 2020), 157–168. doi:10.1007/s41095-020-0167-7

Weiheng Lin, Beibei Wang, Jian Yang, Lu Wang, and Ling-Qi Yan. 2021. Path-based Monte Carlo Denoising Using a Three-Scale Neural Network. *Computer Graphics Forum* 40, 1 (Feb. 2021), 369–381. doi:10.1111/cgf.14194

Yifan Lu, Siyuan Fu, Xiao Hua Zhang, and Ning Xie. 2021. Denoising Monte Carlo renderings via a multi-scale featured dual-residual GAN. *The Visual Computer* 37, 9 (Sept. 2021), 2513–2525. doi:10.1007/s00371-021-02204-4

Yifan Lu, Ning Xie, and Heng Tao Shen. 2020. DMCN-GAN: Adversarial Denoising for Monte Carlo Renderings with Residual Attention Networks and Hierarchical Features Modulation of Auxiliary Buffers. In *SIGGRAPH Asia 2020 Technical Communications*. Association for Computing Machinery, 1–4. doi:10.1145/3410700.3425426

O. L. Mangasarian. 1965. Pseudo-Convex Functions. *Journal of the Society for Industrial and Applied Mathematics Series A Control* 3, 2 (Jan. 1965), 281–290. doi:10.1137/0303020 Publisher: Society for Industrial and Applied Mathematics.

Xiaoxu Meng, Quan Zheng, Amitabh Varshney, Gurprit Singh, and Matthias Zwicker. 2020. Real-time Monte Carlo Denoising with the Neural Bilateral Grid. In *Eurographics Symposium on Rendering (EGSR)*. The Eurographics Association. doi:10.2312/sr.2020201133

Jacob Munkberg and Jon Hasselgren. 2020. Neural Denoising with Layer Embeddings. In *Computer Graphics Forum*, Vol. 39, 1–12. doi:10.1111/cgf.14049

Geunwoo Oh and Bochang Moon. 2024. Joint self-attention for denoising Monte Carlo rendering. *The Visual Computer* 40, 7 (July 2024), 4623–4634. doi:10.1007/s00371-024-03446-8

Matt Pharr, Wenzel Jakob, and Greg Humphreys. 2023. *Physically Based Rendering, fourth edition: From Theory to Implementation*. MIT Press. <https://pbrt.org/>

Tiberiu Popoviciu. 1935. Sur les équations algébriques ayant toutes leurs racines réelles. *Mathematica* 9, 129–145 (1935), 20.

Erik Reinhard, Wolfgang Heidrich, Paul Debevec, Sumanta Pattanaik, Greg Ward, and Karol Myszkowski. 2010. *High Dynamic Range Imaging: Acquisition, Display, and Image-Based Lighting*. Morgan Kaufmann.

Dan Robitzski. 2019. A startup is suing Facebook, Princeton for stealing its AI data. <https://futurism.com/tech-suing-facebook-princeton-data>

Fabrice Rouselle, Claude Knous, and Matthias Zwicker. 2011. Adaptive sampling and reconstruction using greedy error minimization. In *ACM Transactions on Graphics (TOG)*, Vol. 30. ACM, 159. doi:10.1145/2024156.2024193

Fabrice Rouselle, Claude Knous, and Matthias Zwicker. 2012. Adaptive rendering with non-local means filtering. *ACM Transactions on Graphics* 31, 6 (Nov. 2012), 195:1–195:11. doi:10.1145/2366145.2366214

Pradeep Sen and Soheil Darabi. 2012. On filtering the noise from the random parameters in Monte Carlo rendering. *ACM Transactions on Graphics* 31, 3 (May 2012), 1–15. doi:10.1145/2167076.2167083

Shuran Song, Fisher Yu, Andy Zeng, Angel X. Chang, Manolis Savva, and Thomas Funkhouser. 2017. Semantic Scene Completion from a Single Depth Image. In *Proceedings of the IEEE Conference on Computer Vision and Pattern Recognition (CVPR)*. 1746–1754. doi:10.1109/CVPR.2017.28

Andrew Timits. 2022. *Learning Sample-Based Monte Carlo Denoising from Noisy Training Data*. Master's thesis, University of Waterloo, Waterloo, Ontario, Canada. <http://hdl.handle.net/10012/18071>

Vaibhav Vavilala, Rahul Vasanth, and David Forsyth. 2024. Denoising Monte Carlo Renders With Diffusion Models. doi:10.48550/arXiv.2404.00491

Thijs Vogels, Fabrice Rouselle, Brian McWilliams, Gerhard Röthlin, Alex Harvill, David Adler, Mark Meyer, and Jan Novák. 2018. Denoising with Kernel Prediction and Asymmetric Loss Functions. *ACM Transactions on Graphics* 37, 4 (July 2018), 124:1–124:15. doi:10.1145/3197517.3201388

Zhou Wang, Alan Conrad Bovik, Hamid Rahim Sheikh, and Eero P. Simoncelli. 2004. Image quality assessment: from error visibility to structural similarity. *IEEE Transactions on Image Processing* 13, 4 (April 2004), 600–612. doi:10.1109/TIP.2003.819861

Kin-Ming Wong and Tien-Tsin Wong. 2019. Deep residual learning for denoising Monte Carlo renderings. *Computational Visual Media* 5, 3 (Sept. 2019), 239–255. doi:10.1007/s41095-019-0142-3

Bing Xu, Junfei Zhang, Rui Wang, Kun Xu, Yong-Liang Yang, Chuan Li, and Rui Tang. 2019. Adversarial Monte Carlo denoising with conditioned auxiliary feature modulation. *ACM Transactions on Graphics* 38, 6 (Nov. 2019), 224:1–224:12. doi:10.1145/3355089.3356547

Zilin Xu, Qiang Sun, Lu Wang, Yanning Xu, and Beibei Wang. 2020. Unsupervised Image Reconstruction for Gradient-Domain Volumetric Rendering. *Computer Graphics Forum* 39, 7 (2020), 193–203. doi:10.1111/cgf.14137

Xin Yang, Dawei Wang, Wenbo Hu, Lijing Zhao, Xinglin Piao, Dongsheng Zhou, Qiang Zhang, Baocai Yin, Qiang Cai, and Xiaopeng Wei. 2018. Fast Reconstruction for Monte Carlo Rendering Using Deep Convolutional Networks. *IEEE Access* 7 (Dec. 2018), 21177–21187. doi:10.1109/ACCESS.2018.2886005

Xin Yang, Dawei Wang, Wenbo Hu, Li-Jing Zhao, Bao-Cai Yin, Qiang Zhang, Xiao-Peng Wei, and Hongbo Fu. 2019. DEMC: A Deep Dual-Encoder Network for Denoising Monte Carlo Rendering. *Journal of Computer Science and Technology* 34 (Sept. 2019), 1123–1135. doi:10.1007/s11390-019-1964-2

Jiaqi Yu, Yongwei Nie, Chengjiang Long, Wenju Xu, Qing Zhang, and Guiqing Li. 2021. Monte Carlo denoising via auxiliary feature guided self-attention. *ACM Transactions on Graphics (TOG)* 40, 6 (Dec. 2021), 1–13. doi:10.1145/3478513.3480565

Matthias Zwicker, Wojciech Jarosz, Jaakko Lehtinen, Bochang Moon, Ravi Ramamoorthi, Fabrice Rouselle, Pradeep Sen, Cyril Soler, and Sung-Eui Yoon. 2015. Recent Advances in Adaptive Sampling and Reconstruction for Monte Carlo Rendering. *Computer Graphics Forum (Proceedings of Eurographics - State of the Art Reports)* 34, 2 (May 2015), 667–681. doi:10.1111/cgf.12592

A Appendix

A.1 $J(y)$ Functions

The $J(y)$ functions for all combinations of the loss functions introduced in Section 4.1 and the tone mapping functions introduced in Section 5.2 can be found in Table 2. In most cases, since $\varphi'(\hat{y})$ was either convex or concave as shown by $\varphi''(\hat{y})$ being either nonnegative or nonpositive, we were able to use Lemma 1 of Liao and Berg [2019] to easily calculate the $J(y)$ functions as limits of $h(x, y)$. In all of these cases, we had $\lim_{x \rightarrow \infty} h(x, y) = 0$, and $\lim_{x \rightarrow 0} h(x, y)$ gave the single $J(y)$ function. However, there were also several cases where $\varphi'(\hat{y})$ was not convex or concave, and so we had to solve for $\inf_{x \in (0, \infty)} h(x, y)$ and $\sup_{x \in (0, \infty)} h(x, y)$ directly. In these cases, there was both a $J_-(y)$ and a $J_+(y)$ function. In each case, one of these functions was again found at $\lim_{x \rightarrow 0} h(x, y)$. For the other $J(y)$ function, we solved $\frac{\partial}{\partial x} h(x, y) = 0$ for x to find the single critical point, verified that the critical point was the single global minimum or maximum using a first partial derivative test for pseudoconvexity as in Section 4.1, and then substituted that x value into $h(x, y)$. The * entries in Table 2 represent instances where we were unable to solve $\frac{\partial}{\partial x} h(x, y) = 0$ analytically. In these instances, we were still able to find the $J_+(y)$ values numerically, and these results are included in Figure 2(b).

A.2 Finite Data

We now derive a result for finite data similar to the one in Section 3 of the Noise2Noise Supplemental Material [Lehtinen et al. 2018], but adapted for our nonlinear Noise2Noise method. We have N clean targets y_i , N noisy targets \hat{y}_i , and N error terms e_i for a finite number N . The \hat{y}_i are random variables defined such that each $\mathbb{E}[\hat{y}_i] = y_i$, and the e_i are random variables that model the error introduced by the nonlinearity of the loss function. The expected squared error between the means of the y_i and $(\hat{y}_i + e_i)$ terms is then

$$\begin{aligned} & \mathbb{E} \left[\left(\frac{1}{N} \sum_i y_i - \frac{1}{N} \sum_i (\hat{y}_i + e_i) \right)^2 \right] \\ &= \frac{1}{N^2} \left(\left(\sum_i y_i \right)^2 - 2 \left(\sum_i y_i \right) \mathbb{E} \left[\sum_i (\hat{y}_i + e_i) \right] + \mathbb{E} \left[\left(\sum_i (\hat{y}_i + e_i) \right)^2 \right] \right) \\ &= \frac{1}{N^2} \left(\left(\sum_i y_i \right)^2 - 2 \left(\sum_i y_i \right) \mathbb{E} \left[\sum_i \hat{y}_i \right] - 2 \left(\sum_i y_i \right) \mathbb{E} \left[\sum_i e_i \right] \right. \\ & \quad \left. + \mathbb{E} \left[\left(\sum_i \hat{y}_i \right)^2 \right] + 2 \mathbb{E} \left[\sum_i \hat{y}_i \sum_i e_i \right] + \mathbb{E} \left[\left(\sum_i e_i \right)^2 \right] \right) \\ &= \frac{1}{N^2} \left(\text{Var} \left(\sum_i \hat{y}_i \right) + 2 \text{Cov} \left(\sum_i \hat{y}_i, \sum_i e_i \right) \right. \\ & \quad \left. + \text{Var} \left(\sum_i e_i \right) + \mathbb{E} \left[\sum_i e_i \right]^2 \right) \\ &= \frac{1}{N^2} \left(\text{Var} \left(\sum_i (\hat{y}_i + e_i) \right) + \mathbb{E} \left[\sum_i e_i \right]^2 \right) \end{aligned}$$

$$\begin{aligned} &= \frac{1}{N} \left(\frac{1}{N} \sum_i \sum_j \text{Cov}(\hat{y}_i + e_i, \hat{y}_j + e_j) \right) + \left(\frac{1}{N} \sum_i \mathbb{E}[e_i] \right)^2 \\ &= \frac{1}{N} \left(\frac{1}{N} \sum_i \text{Var}(\hat{y}_i + e_i) \right) + \left(\frac{1}{N} \sum_i \mathbb{E}[e_i] \right)^2, \end{aligned}$$

where the last line is a simplification that is valid when the $(\hat{y}_i + e_i)$ terms are uncorrelated. We can see from the last two lines above that the expected error is composed of two overall terms: a variance term and a bias term. The error from training with noisy targets \hat{y}_i occurs entirely in the variance term, because the noisy targets have the correct mean $\mathbb{E}[\hat{y}_i] = y_i$. This average variance term decreases as the number of samples increases. The error from the nonlinearity of the loss function e_i occurs in both the variance and bias terms. The variance component decreases as the number of samples increases, while the bias component does not vary with the number of samples.

A.3 Additional Qualitative Results

Figure 6 shows some additional copies of Figure 4 featuring different validation images. These images provide further evidence for the findings in Section 5.2. Figure 7 shows some additional outputs from our models and SBMC on example images from the SBMC test set. The first scene involves rotating spheres with motion blur hovering over a mirror. The zoomed-in portion shows one of the spheres with specular highlights and blurred textures, where the outputs from our models are similar to that of SBMC and to the reference image. The second scene contains a complicated metallic structure that is suspended over a reflective surface. The zoomed-in portion shows that our models again produce similar output to SBMC, capturing the details of the structure but missing some small areas of shadow. Both our models and SBMC over-blur some of the reflection of the structure. The third scene shows a Cornell box with matte, reflective, and refractive objects. The zoomed-in portion shows that the reference image is still quite noisy. All models produce outputs that are visually better than the reference image, with our models producing smaller caustics than SBMC. Both our models and SBMC over-blur the reflection of the purple sphere and miss a highlight on the glass sphere. The fourth scene features a house model in outdoor lighting conditions. The zoomed-in portion shows that our models over-blur the railing, producing outputs that are less sharp than SBMC. Our models also over-blur the window frame above the railing, although all of the models distort the part of the window frame that is visible through the railing. The fifth scene shows a classroom with light streaming in through the windows. The zoomed-in portion shows that the outputs are similar between our models and SBMC, although our models slightly over-blur the chair feet and the point of the shadow on the floor. The final scene is a bathroom lit by a diffuse light source on the far wall. The zoomed-in portion shows that our models produce similar output to SBMC, but miss some detail in the wood texture and in the reflection of the floor in the trash can. Both our models and SBMC over-blur the floor texture where it is in shadow.

Table 2. $J(y)$ functions for various combinations of tone mapping and loss functions. A blank space means that the function is $J(y) = 0$. See Section A.1 for details on the * values.

| $\varphi(\hat{y})$ | $J_-(y)$ | $J_+(y)$ |
|--|---|--|
| $T_R = \frac{\hat{y}}{1+\hat{y}}$ | $-\frac{1}{(y+1)^2}$ | |
| $T_G = \hat{y}^{\frac{1}{2.2}}$ | $-\frac{6}{11y^{\frac{17}{11}}}$ | |
| $T_{RG} = T_G \circ T_R$ | $-\frac{11y^{+6}}{11y^{\frac{17}{11}}(y+1)^{\frac{16}{11}}}$ | |
| $\frac{1}{(\hat{y}+\epsilon)^2}$ | | $\frac{3\epsilon+y}{\epsilon^2(\epsilon+y)^3}$ |
| $\frac{\hat{y}}{(\hat{y}+\epsilon)^2}$ | $-\frac{2}{(\epsilon+y)^3}$ | $\frac{(-\epsilon+y)^2}{4\epsilon(\epsilon+y)^4}$ |
| $\frac{1}{(T_R+\epsilon)^2}$ | | $\frac{2\epsilon^2y+2\epsilon^2+3\epsilon y+3\epsilon+y}{\epsilon^2(\epsilon y+\epsilon+y)^3}$ |
| $\frac{T_R}{(T_R+\epsilon)^2}$ | $-\frac{\epsilon y+\epsilon+y+2}{(\epsilon y+\epsilon+y)^3}$ | $\frac{(\epsilon+1)^2(\epsilon y+\epsilon-y)^2}{4\epsilon(\epsilon y+\epsilon+y)^4}$ |
| $\frac{1}{(T_G+\epsilon)^2}$ | | $\frac{12\epsilon^2y+33\epsilon y^{\frac{16}{11}}+11y^{\frac{21}{11}}}{11\epsilon^2y^{\frac{28}{11}}\left(\epsilon+y^{\frac{5}{11}}\right)^3}$ |
| $\frac{T_G}{(T_G+\epsilon)^2}$ | $-\frac{2\left(3\epsilon y+8y^{\frac{16}{11}}\right)}{11y^{\frac{28}{11}}\left(\epsilon+y^{\frac{5}{11}}\right)^3}$ | * |
| $\frac{1}{(T_{RG}+\epsilon)^2}$ | | $\frac{22\epsilon^2y^2+12\epsilon^2y+33\epsilon y^{\frac{16}{11}}(y+1)^{\frac{6}{11}}+11y^{\frac{21}{11}}(y+1)^{\frac{1}{11}}}{11\epsilon^2y^{\frac{28}{11}}(y+1)^{\frac{1}{11}}\left(\epsilon(y+1)^{\frac{5}{11}}+y^{\frac{5}{11}}\right)^3}$ |
| $\frac{T_{RG}}{(T_{RG}+\epsilon)^2}$ | $-\frac{11\epsilon y^2(y+1)^{\frac{5}{11}}+6\epsilon y(y+1)^{\frac{5}{11}}+11y^{\frac{27}{11}}+16y^{\frac{16}{11}}}{11y^{\frac{28}{11}}(y+1)^{\frac{6}{11}}\left(\epsilon(y+1)^{\frac{5}{11}}+y^{\frac{5}{11}}\right)^3}$ | * |
| T_R^2 | $-\frac{y^2}{(y+1)^4}$ | $\begin{cases} \frac{1-y}{(y+1)^3} & 0 \leq y \leq 1 \\ 0 & 1 \leq y \end{cases}$ |
| T_G^2 | $-\frac{1}{11y^{\frac{12}{11}}}$ | |
| T_{RG}^2 | $-\frac{11y+1}{11y^{\frac{12}{11}}(y+1)^{\frac{21}{11}}}$ | |

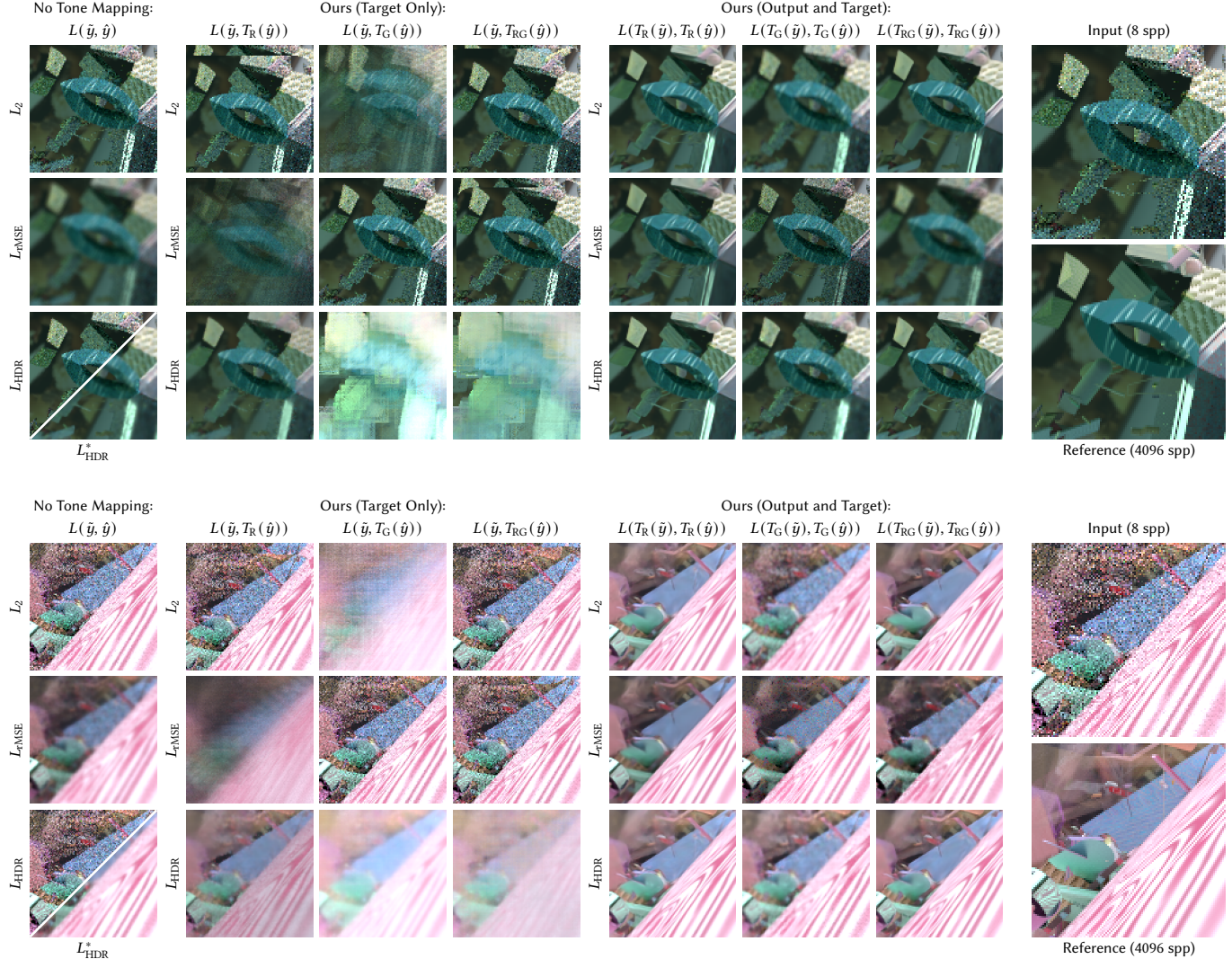


Fig. 6. Model outputs for a single validation image for all combinations of loss functions, tone mapping functions, and tone mapping placement

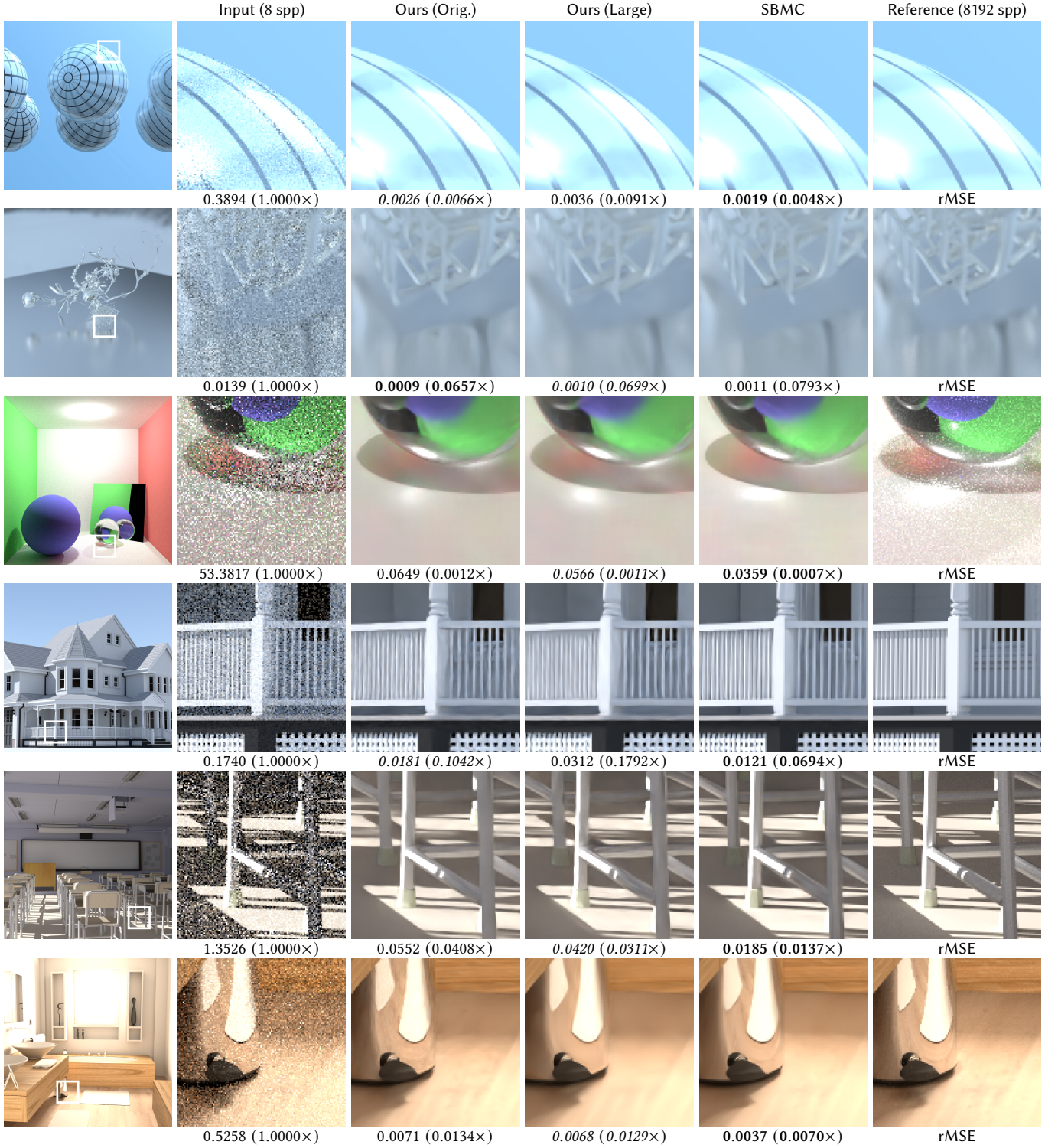


Fig. 7. Comparison between the outputs of our denoising models and SBMC on several test images. Columns from left to right: overview of the test image with the crop region outlined, noisy input rendered at 8 samples per pixel (spp), output of our original denoising model, output of our large denoising model, SBMC output, and reference image rendered at 8192 spp. (anim-bluespheres Copyright ©1998-2012, Matt Pharr and Greg Humphreys; Yeah Right by Keenan Crane, CC0 1.0; GITestSynthesizer_01 Copyright ©2019, Michaël Gharbi; Victorian Style House by MrChimp2313, CC0 1.0; Japanese Classroom by NovaAshbell, CC BY 3.0; Bathroom by nacimus, CC BY 3.0)